Supporting Information

Mesoporous PdAgIr Nanoalloys to Electrocatalysize the Formate Oxidation with Unprecedentedly Low Onset Potential

Yachao, Jin[a, b] *Fuyi Chen** [a, b] *Tao Jin,* [a, b] *Longfei Guo,* [a, b] *and Jiali Wang** [a, b]

[a] State Key Laboratory of Solidification Processing, Northwestern Polytechnical University, Xi'an 710072, China.

[b] School of Materials Science and Engineering, Northwestern Polytechnical University, Xi'an, 710072, China.

Methods

Density Functional Theoretical (DFT) calculation: The theoretical study in this work was conducted by DFT with the atomic orbital-based DMol^3 package.[1] The Perdew-Becke-Ernzerhof (PBE) in the generalized gradient approximation (GGA) was used as the exchange and correlation functional. [2] The convergence tolerance of energy was 2×10^{-5} Ha, maximum force was 0.004 Ha Å^{-1}, and maximum displacement was 0.005 Å. The electrons of heavy metal atoms (Ag, Pd, Ir) were treated with Density functional Semi-core Pseudo-Potentials (DSPP). The unit cell used 3 × 3 × 3, and the slab model used 3 × 3 × 1 k-point sampling of the Brillouin zone type for Brillouin zone integration. Smearing populates the energy levels around the Fermi level according to a thermal distribution and can help to improve SCF convergence. Here, thermal smearing of 0.005 Ha (1Ha = 27.2114 eV) was used to speed up SCF convergence. The slab model of the catalyst surface was modeled by using four layers composed of 3 × 3 supercell. The two layers of atoms at the bottom of the Slab model are fixed to simulate the catalyst block, and the other atoms are completely relaxed to simulate the catalyst surface. A vacuum space of 15 Å was used to prevent artificial interaction effect between the slab and their mirror images. All adsorption sites take the lowest adsorption energy site.[1, 2]

Chemicals: Sodium tetrachloropalladate (Na_2PdCl_4), hydrogen hexachloroiridate (H_2IrCl_6) hexadecylpyridinium chloride monohydrate ($C_5H_5N(Cl)(CH_2)_{15}CH_3\cdot H_2O$, HDPC). Ascorbic acid ($C_6H_8O_6$, AA), potassium hydrate (KOH), potassium formate (HCOOK) and ethanol were all purchased from Sinopharm Chemical Reagent Co. Ltd. All chemicals were analytical grade and employed as received without any purification. The ultrapure water (>18.25 MΩ cm) was employed to prepare all the solution.

Synthesis of PdAgIr NFs: In a typical synthesis of PdAgIr NFs, 0.018 g hexadecylpyridinium chloride monohydratean (HDPC) as surfactant was firstly dissolved into 5 mL ultrapure water under gentle stirring. Then, the precursors of sodium tetrachloropalladate (Na_2PdCl_4, 0.27 mL, 10 mM), hydrogen hexachloroiridate (H_2IrCl_6, 0.18 mL, 10 mM) and silver nitrate ($AgNO_3$, 0.13 mL, 10 mM) were sequentially added into above solution. After 10 min of stirring for homogeneous mixing, a freshly prepared ascorbic acid (AA, 0.3 mL, 100 mM) solution as reducing agent was quickly injected, and the resulting mixture was kept statically at 35 °C for 3h. The as-prepared products were collected by centrifugation and rinsed by ultrawater and ethaol for several times. The final PdAgIr NFs solid products were obtained by freeze-dried process for 12 h. On the other hand, to prepare other nanomaterials, including $PdAgIr_2$ NFs, $PdAgIr_7$ NFs, $PdIr_6$ NFs, PdAg NFs and Pd NFs,

the identical methodology was utilized with only changing the precursor amounts and species.[3]

Physical characterizations: The phase structure of as-synthesized samples were investigated by X-ray diffraction (XRD) patterns conducted on a PANalytical X'Pert Pro MPD with Cu Kα radiation (λ = 1.5406 Å). Transmission electron microscopy (TEM) images were performed on an FEI Talos F200X with an accelerating voltage of 200 kV. High-angle annular dark-field scanning transmission electron microscopy (HAADF-STEM) images coupled with X-ray energy-dispersive spectroscopy (EDS) were carried out to study the elemental distribution among the samples. The inductively coupled plasma-optical emission spectrometry (ICP-OES) was conducted to analyze the composition. X-ray photoelectron spectroscopy (XPS) was obtained on an ESCALAB 250 instrument with an ultrahigh vacuum (10^{-9} Torr) using monochromated Al Kα radiation (hν = 1486.6 eV); And all the binding energies were calibrated by the carbon peak (C 1s) at about 284.5 eV. The d-band center was calculated on the basis of to the formula in the range of 0 and −9 eV: $\int N(\varepsilon)\ \varepsilon\ d\varepsilon\ /\ N(\varepsilon)\ d\varepsilon$, where N(ε) is the density of states (DOS), and all the spectra were corrected by means of the Shirley background.

Electrochemical measurements: All electrochemical experiments were conducted with a conventional three-electrode cell on the CHI 660C electrochemical workstation. The glassy carbon electrode (GCE, 5 mm), platinum gauze and Hg/HgO electrode were taken as the working, counter and reference electrodes, respectively. All potentials recorded in this experiment were scaled versus the reversible hydrogen electrode (RHE) by the following formula: $E_{RHE} = E_{Hg/HgO} + 0.098\ V + 0.059 \times pH$. The GCE electrode was successively polished by 0.3 and 0.05 μm alumina powder and ultrasonically cleaned in acetone and water before the electrocatalysts coating. Typically, to prepare the electrocatalysts slurry, 1 mg of as-prepared electrocatalysts and 4 mg Vulcan XC-72 carbon were dispersed in 1.97 mL of ethanol and 30 μL of 5 wt% Nafion solution, which was then ultrosonicated for an hour to form a uniform electrocatalyst suspension. 10 μL of the electrocatalyst suspension was dropped onto the GCE surface and dried naturally. For comparison, the commercial Pd/C electrocatalyst (Pd 10 wt%) was prepared by the same method. The electrochemically active surface area (ECSA) of various nanomaterials were examined by Cu underpotential deposition (Cu upd). Specifically, the GCE electrodes modified with as-prepared nanomaterials were firstly polarized at 0.3 V for 60 s. A linear voltammetric scan was then performed from the admission potential to a point at which all the upd copper had been oxidized at a scan rate of 0.01 V s^{-1}. The formula to determine the ECSAs is described as following equation:

$$ECSA = Q_{Cu} / (C \times m) = RF / m$$

Where Q_{Cu} represents the upd Cu stripping charge, m is the Pd mass loading, the C value is a constant of 0.47 mC cm^{-2}, $RF = Q_{Cu} / C$ represents the roughness factor (RF). Conventionally, the formate oxidation reaction (FOR) experiments were carried out in 1 M KOH + 1 M HCOOK solution with a scan rate of 50 mV s^{-1} at the potential window of 0.024 ~ 1.1 V (vs RHE).

The direct formate fuel cells (DFFCs) were fabricated by using a home-made fuel cell mode. The as-prepared catalysts and commercial Pt/C (20%) were used as the anodic and cathodic catalysts with a fixed metal loading of 1 mg cm^{-1}_{metal}, respectively. The anion-exchange membrane with thickness of 15 μm was used as the alkaline electrolyte membrane, which was pretreated in 2 M KOH solution for 24 h. The anodic electrolyte of 4 M HCOOK + 4 M KOH solution were directly fed to the anode at approximately 1 mL min^{-1}. The pure oxygen was directly fed to the cathodic side at approximately 100 sccm. The DFFCs were operated at 25 °C. For the voltage-current experiments, the DFFCs were stepped from open circuit voltage to approximately 0.35 V.

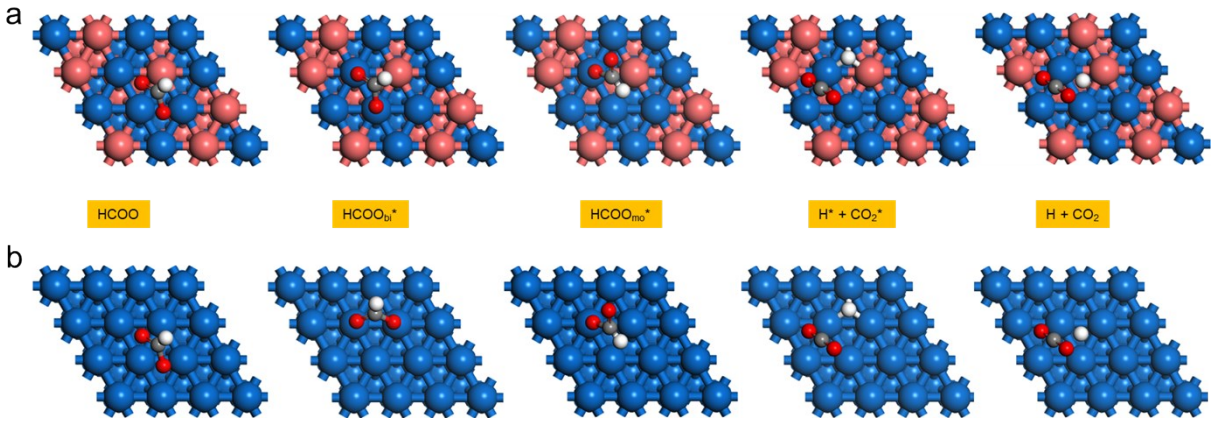

Fig. S1. Adsorption configurations of the FOR intermediates on (a) PdAg (111) and (b) Pd (111) surfaces, respectively. The blue, pink, yellow, gray, red and white balls represent the Pd, Ag, Ir, C, O and H atoms, respectively;

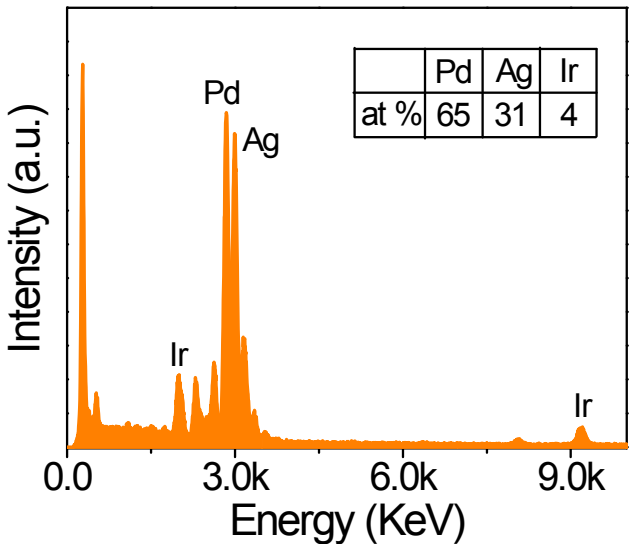

Fig. S2. EDS spectrum of PdAgIr NFs.

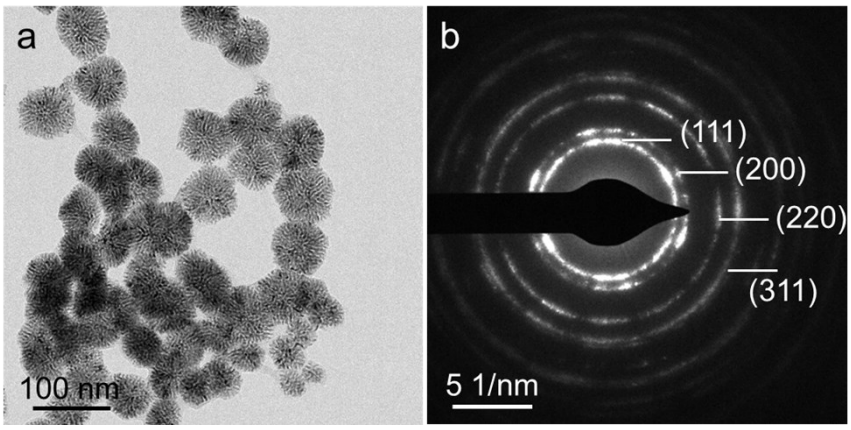

Fig. S3. (a) TEM and (b) SAED images of Pd NFs.

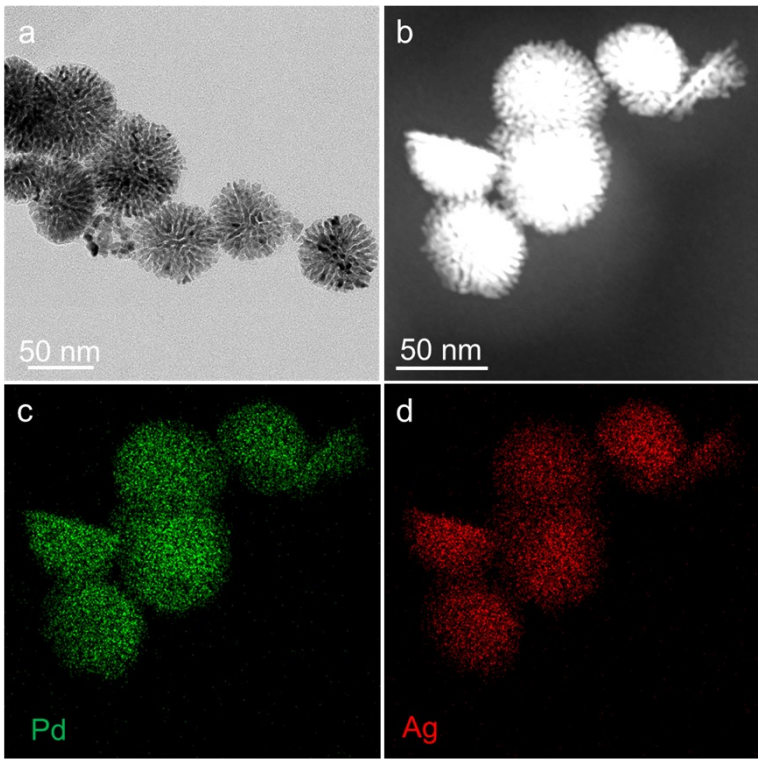

Fig. S4. (a) TEM image; (b) HADDF-STEM image and (c)-(d) corresponding elemental mapping images of PdAg NFs.

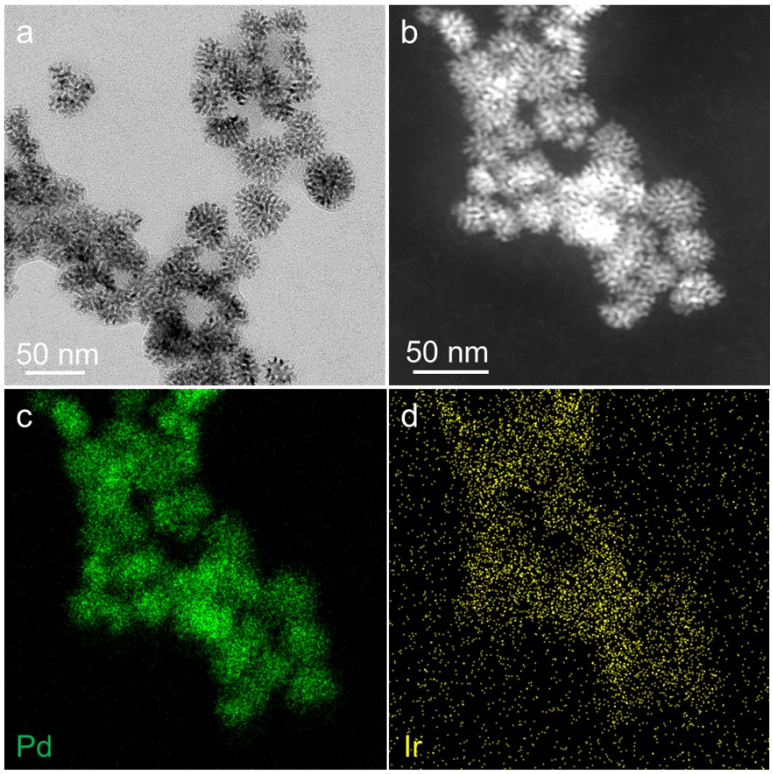

Fig. S5. (a) TEM image; (b) HADDF-STEM image and (c)-(d) corresponding elemental mapping images of PdIr NFs.

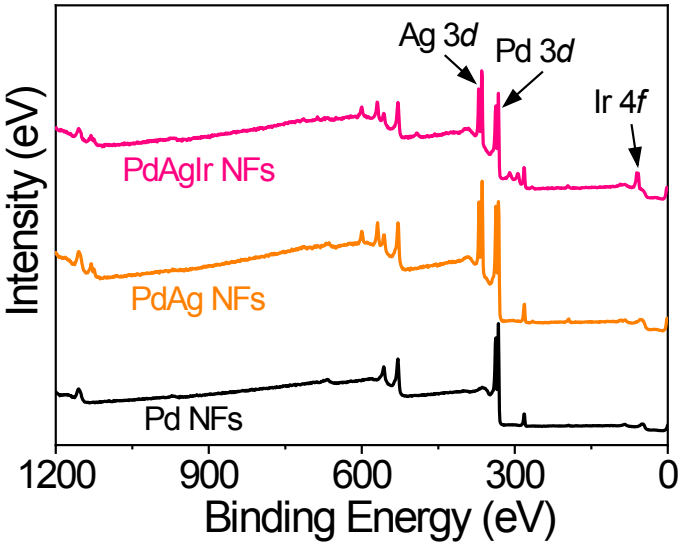

Fig. S6. XPS survey spectra of PdAgIr NFs, PdAg NFs and Pd NFs.

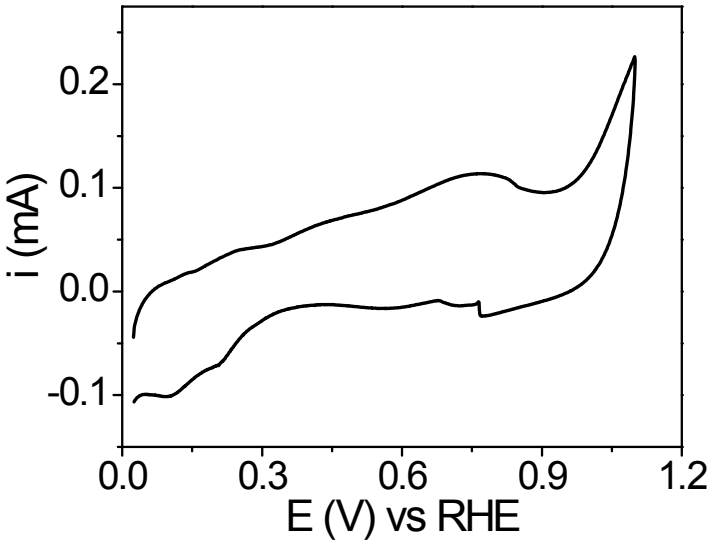

Fig. S7. FOR performance of Ir/C catalysts.

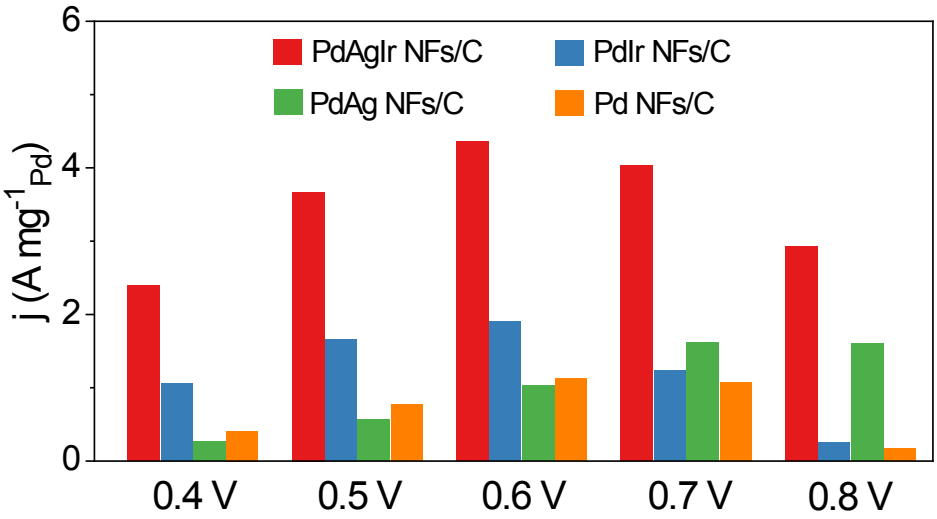

Fig. S8. Comparison of FOR performance for PdAgIr NFs/C, PdIr NFs/C, PdAg NFs/C and Pd NFs/C catalysts at periodically selected potentials of 0.4, 0.5, 0.6, 0.7 and 0.8 V;

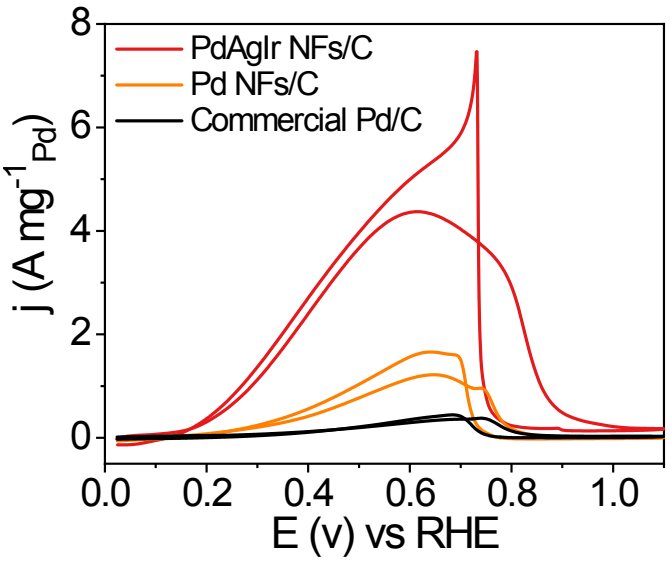

Fig. S9. FOR activity of PdAgIr NFs/C, Pd NFs/C and commercial Pd/C catalysts

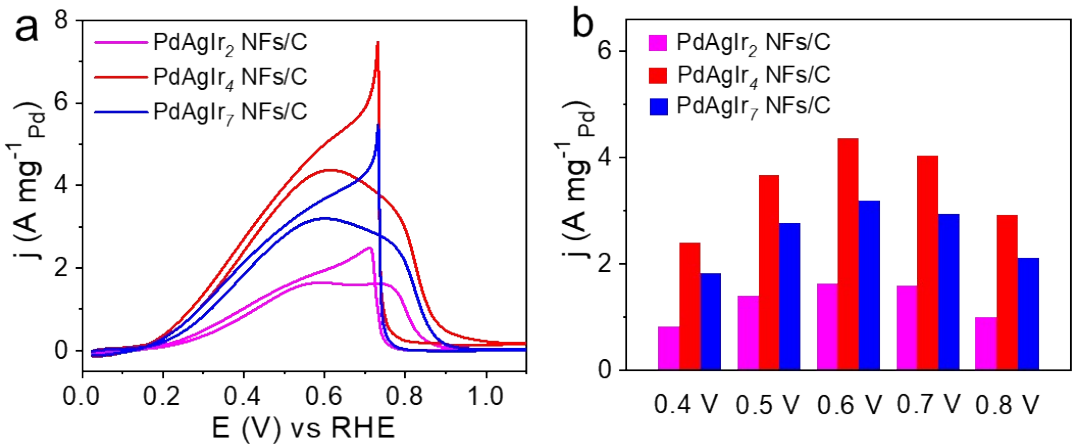

Fig. S10. FOR performance of $PdAgIr_2$ NFs/C, $PdAgIr_4$ NFs/C (PdAgIr NFs/C) and $PdAgIr_7$ NFs/C catalysts.

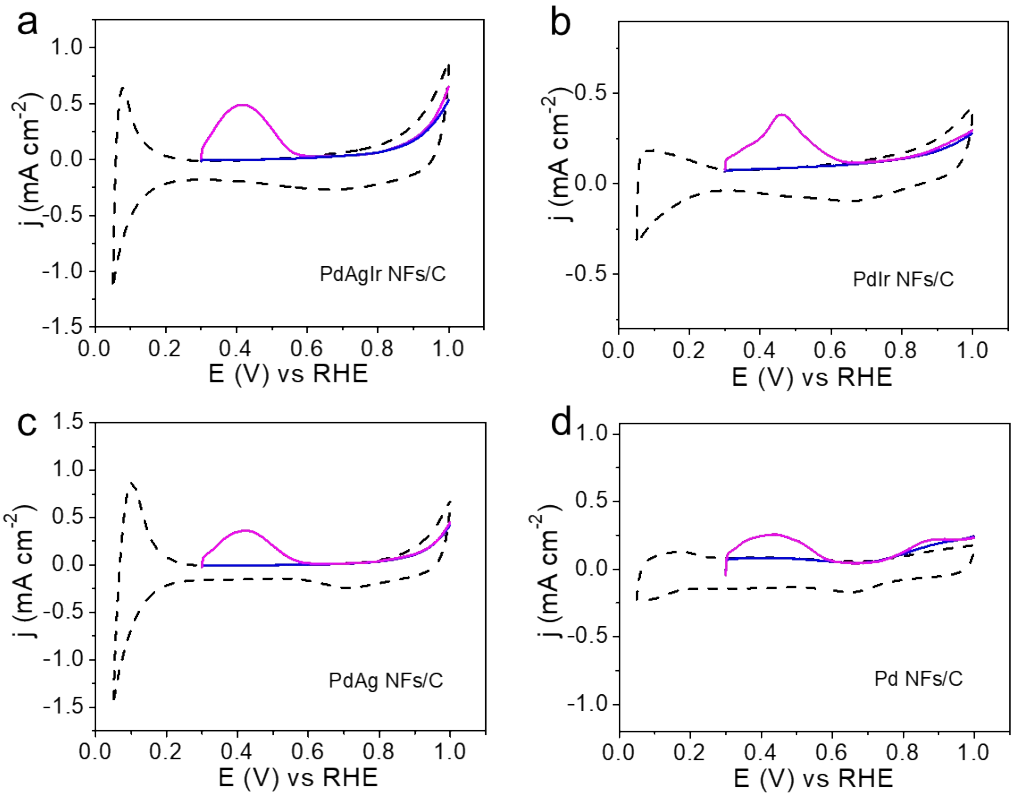

Fig. S11. Cu underpotential deposition of (a) PdAgIr NFs/C, (b) PdIr NFs/C, (c) PdAg NFs/C and (d) Pd NFs/C catalysts.

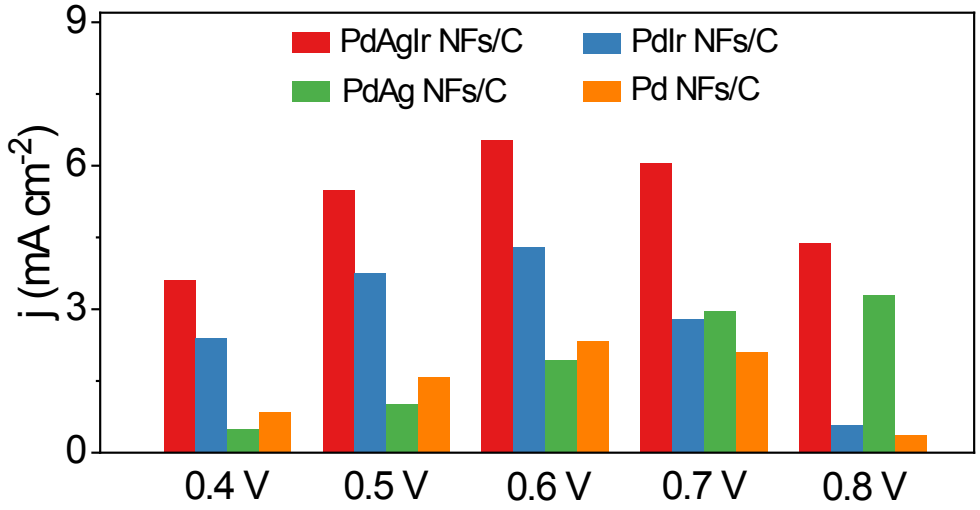

Fig. S12. Specific activity (SA) of FOR for PdAgIr NFs/C, PdIr NFs/C, PdAg NFs/C and Pd NFs/C catalysts.

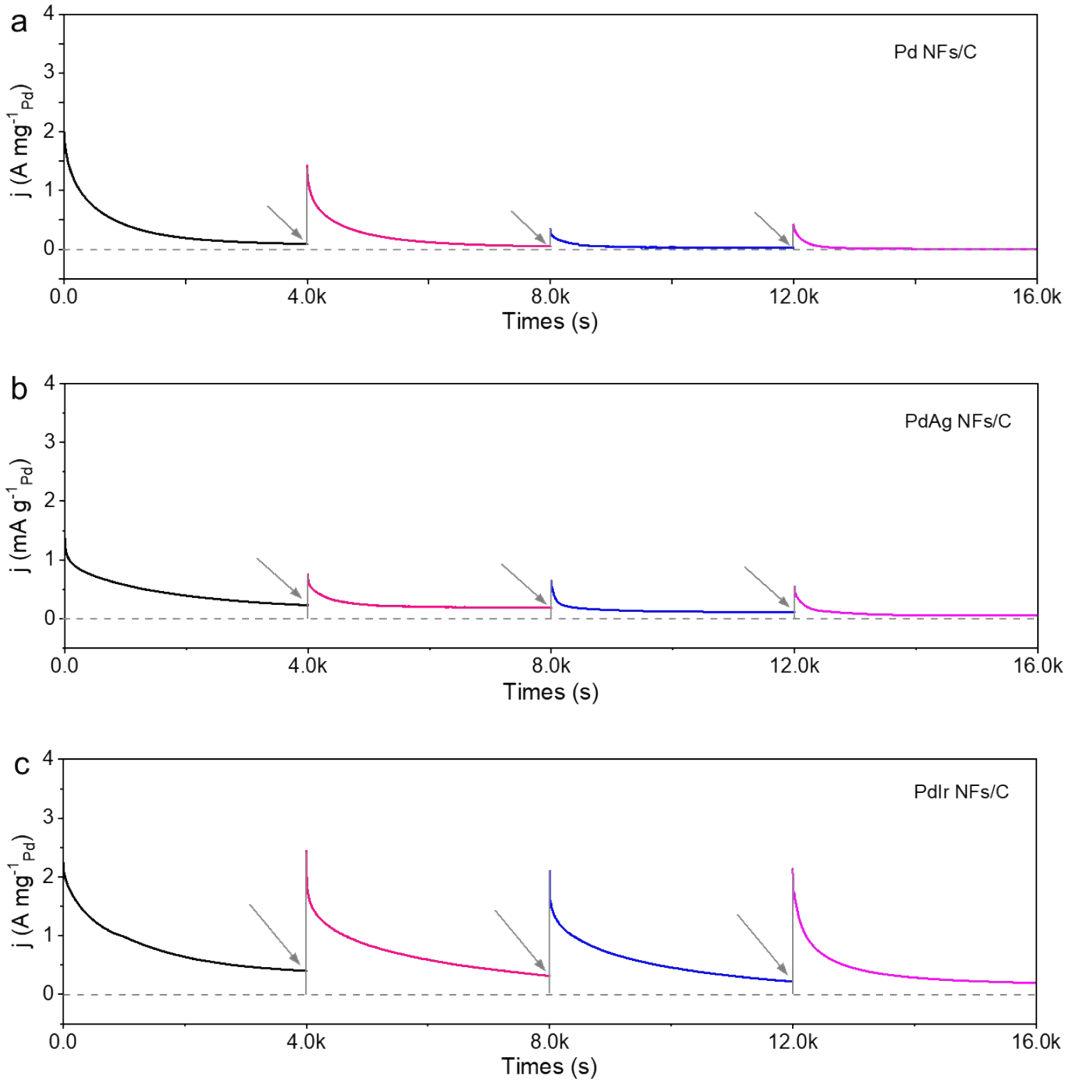

Fig. S13. Recoverability of (a) Pd NFs/C, (b) PdAg NFs/C and (c) PdAgIr NFs/C catalysts.

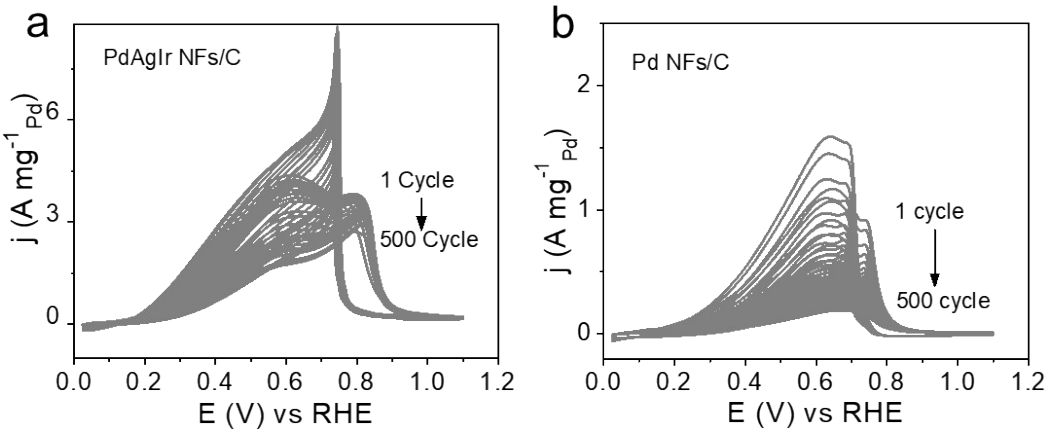

Fig. S14. Cycling stability of (a) PdAgIr NFs/C and (b) Pd NFs/C catalysts for FOR.

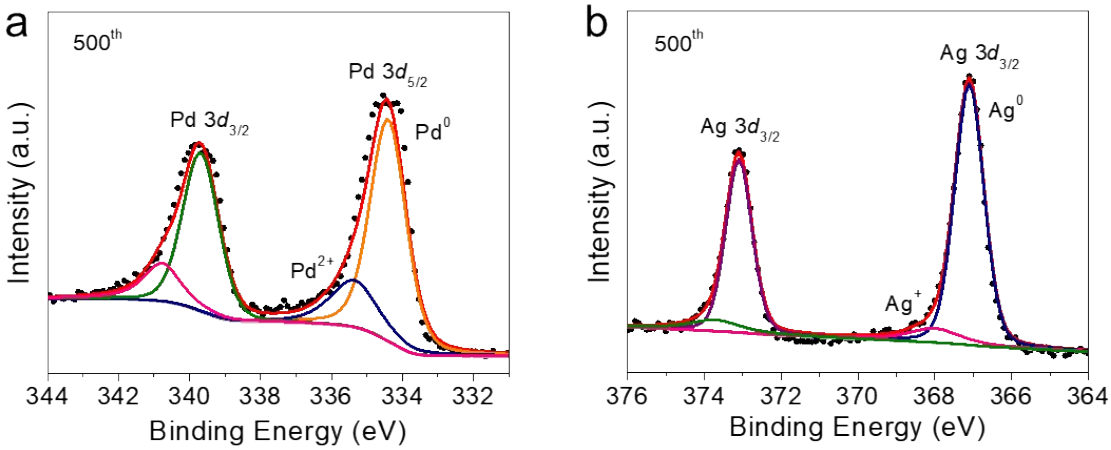

Fig. S15. High resolution XPS spectra of (a) Pd 3d and (b) Ag 3d for PdAgIr NFs/C catalyst after 500 cycles;

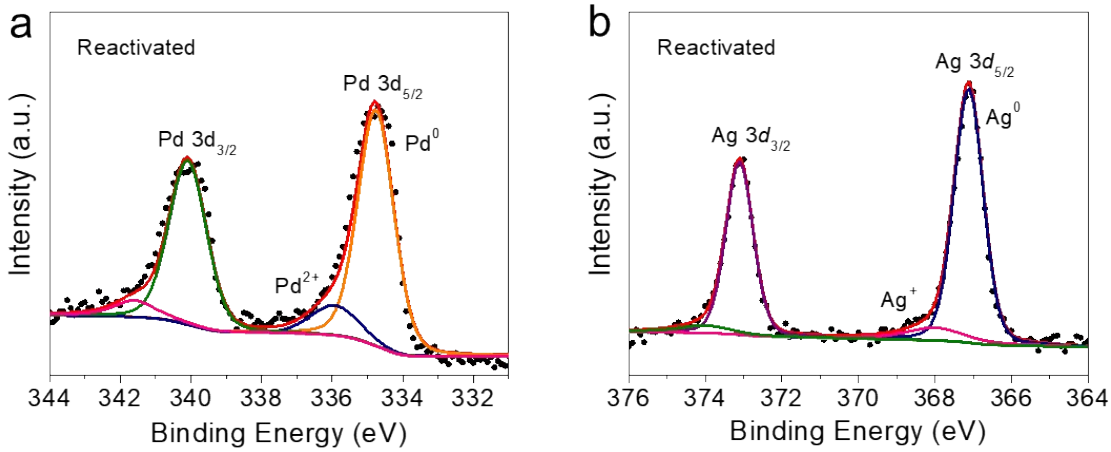

Fig. S16. High resolution XPS spectra of (a) Pd 3d and (b) Ag 3d for PdAgIr NFs/C catalyst after reactivation.

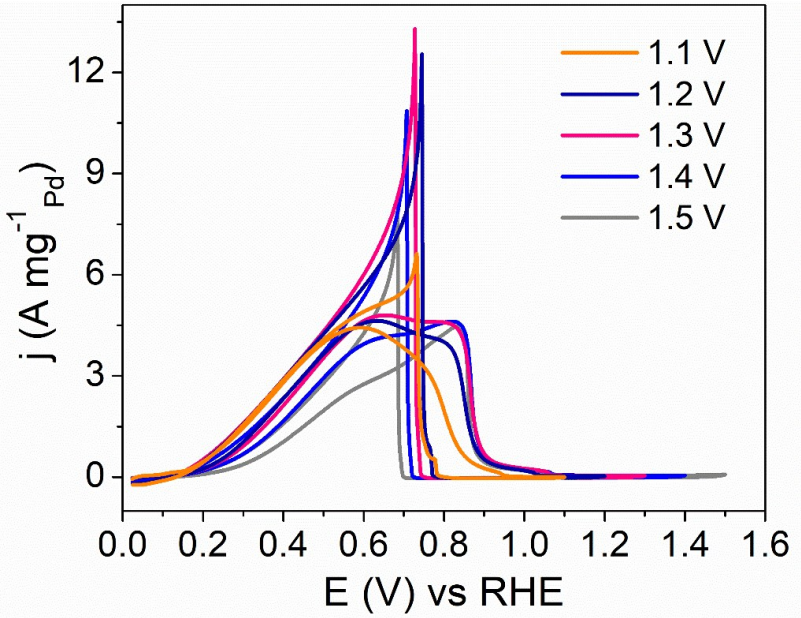

Fig. S17. CV curves of PdAgIr NFs/C catalyst for FOR at different upper limit potentials (ULPs) of 1.1, 1.2, 1.3, 1.4 and 1.5 V.

Fig. S17 shows the FOR performance of PdAgIr NFs/C catalyst at different ULPs. It can be seen that the FOR performance of PdAgIr NFs/C catalyst changes with extending the ULPs. Firstly, as increasing the ULPs from 1.1 V to 1.5 V, the current densities in the potential range of 0.7~0.9 V were enhanced, which is ascribed to the surface reconstruction of PdAIr NFs/C catalyst induced by Ag surface oxide species, in agreement with our previous researches.[4-6] On the other hand, the current densities before 0.7 V gradually decrease with extending the ULPs. In particular, the onset potentials of PdAgIr NFs/C catalyst toward FOR were positively shifted, which is attributable to the robust oxidation of Ir atoms at higher ULPs. Superfluous oxidation of Ir atoms in PdAgIr NFs/C compels such catalyst to lose the alloying effect of Ir, leading to a sluggish catalytic kinetic.

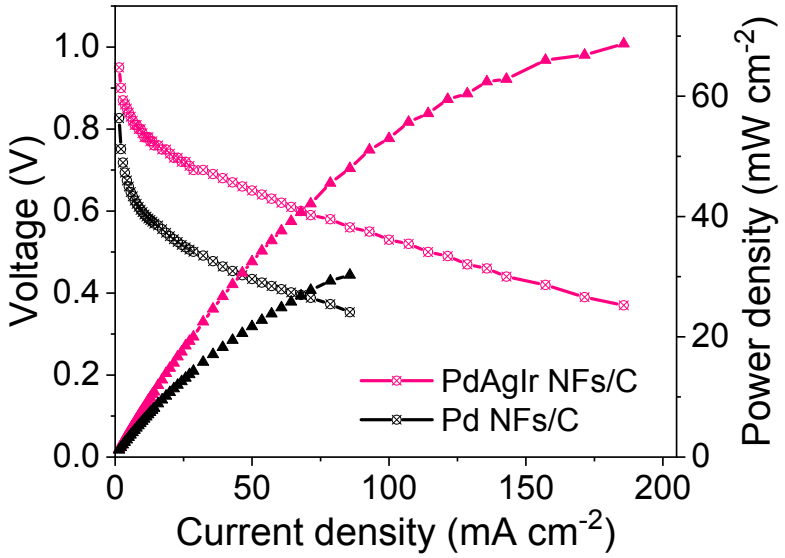

Fig. S18. Polarization and power density curves of DFFCs with PdAgIr NFs/C and Pd NFs/C cathodic catalysts.

Table S1. The atomic and mass ratio of Pd, Ag and Ir elements for different catalysts

catalysts	at%			wt%		
	Pd	Ag	Ir	Pd	Ag	Ir
PdAgIr NFs	65	31	4	63	30	7
$PdAgIr_2$ NFs	66	32	2	65	32	3
$PdAgIr_7$ NFs	65	28	7	61	27	12
PdIr NFs	94	/	6	90	/	10
PdAg NFs	68	32	/	68	32	/

Table S2. Comparison of MA for different catalysts at various potentials.

	0.4 V ($A\ mg^{-1}_{Pd}$)	0.5 V ($A\ mg^{-1}_{Pd}$)	0.6V ($A\ mg^{-1}_{Pd}$)	0.7V ($A\ mg^{-1}_{Pd}$)	0.8 V ($A\ mg^{-1}_{Pd}$)
PdAgIr NFs/C	2.4	3.67	4.36	4.03	2.93
PdIr NFs/C	1.06	1.66	1.9	1.23	0.25
PdAg NFs/C	0.27	0.57	1.03	1.62	1.61
Pd NFs/C	0.41	0.77	1.13	1.07	0.17

Table S3. Comparison of SA for different calysts at various potentials.

	0.4 V ($mA\ cm^{-2}$)	0.5 V ($mA\ cm^{-2}$)	0.6V ($mA\ cm^{-2}$)	0.7V ($mA\ cm^{-2}$)	0.8 V ($mA\ cm^{-2}$)
PdAgIr NFs/C	3.6	5.5	6.54	6.05	4.39
PdIr NFs/C	2.4	3.75	4.3	2.79	0.57
PdAg NFs/C	0.49	1.02	1.93	2.96	3.3
Pd NFs/C	0.85	1.58	2.34	2.1	0.36

Table S4. Ratio of Ir^0/Ir^{4+}, Pd^0/Pd^{2+} and Ag^0/Ag^+ for PdAgIr NFs/C catalysts at different states.

	As-prepared	After 500 cycles	After reactivation
Ir^0	75.3	58.7	69.2
Ir^{4+}	24.7	41.3	30.8
Pd^0	77.4	75.9	85.5
Pd^{2+}	22.6	24.1	14.5
Ag^0	81.2	88.7	89.0
Ag^+	18.8	11.3	11.0

References:

[1] N. Zhang, F. Chen, L. Guo, Catalytic Activity of Palladium-doped Silver Dilute Nanoalloys for Formate Oxidation from a Theoretical Perspective, *Phy. Chem. Chem. Phy.* **2019**, *21*, 22598-22610.

[2] W. Gao, J.A. Keith, J. Anton, T. Jacob, Theoretical Elucidation of the Competitive Electro-oxidation Mechanisms of Formic Acid on Pt(111), *J. Am. Chem. Soc.* **2010**, *132(51)*, 18377-18385.

[3] X. Huang, Y. Li, Y. Chen, E. Zhou, Y. Xu, H. Zhou, X. Duan, Y. Huang, Palladium-Based Nanostructures with Highly Porous Features and Perpendicular Pore Channels as Enhanced Organic Catalysts, *Angew. Chem. Int. Ed.* **2013**, *52(9)*, 2520-2524.

[4] Y. Jin, F. Chen, L. Guo, J. Wang, B. Kou, T. Jin, H. Liu, Engineering Two-Dimensional PdAgRh Nanoalloys by Surface Reconstruction for Highly Active and Stable Formate Oxidation Electrocatalysis, *ACS Appl. Mater. Interfaces* **2020**, *12(23)*, 26694-26703.

[5] L. Guo, F. Chen, T. Jin, H. Liu, N. Zhang, Y. Jin, Q. Wang, Q. Tang, B. Pan, Surface reconstruction of AgPd nanoalloy particles during the electrocatalytic formate oxidation reaction, *Nanoscale* **2020**, *12(5)*, 3469-3481.

[6] J. Wang, F. Chen, Y. Jin, L. Guo, X. Gong, X. Wang, R.L. Johnston, In situ high-potential-driven surface restructuring of ternary AgPd–Ptdilute aerogels with record-high performance improvement for formate oxidation electrocatalysis, *Nanoscale* **2019**, *11(30)*, 14174-14185.